PENINSULA PUBLISHING LLC

KHWARIZMIA
Vol. **(2026)**, 2026, **pp.** 93–109
ISSN: 3078-2694

Research Article

Analytical Modeling for Nonlinear Seismic Metasurfaces of Saturated Porous Media

Dalia Awlad[1,*], Omer H. Alwan[2], Ali Mohammed Rashid[2]

[1] *Transportation department, Al-wataniya private university, Hama, Syria.*

[2] *Computer Science Department, College of Education, Al-Iraqia University, Baghdad, Iraq.*

ARTICLEINFO

Article History

Received 15 May 2026

Revised: 03 Jul 2026
Accepted 01 Aug 2026
Published 16 Aug 2026

Keywords

seismic metasurfaces,

saturated porous media,

Biot theory,

nonlinear wave propagation,

attenuation bandgaps,

sub-wavelength resonators,

pore-pressure dissipation.

ABSTRACT

Background: Rayleigh waves transport the greater part of the energy released by shallow earthquakes and dominate the damage potential of near-surface ground motion. Sub-wavelength resonant metasurfaces offer a route to intercepting this energy before it reaches a protected structure, yet almost all available closed-form treatments idealise the substrate as a dry, linearly elastic half-space.
Problem: Urban sites requiring protection are frequently underlain by shallow water tables, so the substrate is a two-phase medium in which solid–fluid coupling, pore-pressure diffusion and viscous Darcy flow act simultaneously. Under strong shaking the skeleton additionally leaves the small-strain regime, the shear modulus degrades and excess pore pressure accumulates, so both the substrate impedance and the resonator tuning drift during the event.
Method: This work develops a closed-form dispersion theory for a locally resonant metasurface bonded to a Biot fluid-saturated poroelastic half-space. Skeleton nonlinearity is introduced through a strain-compatible Hardin–Drnevich modulus-degradation law coupled to an effective-stress reduction driven by the pore-pressure ratio, and resonator nonlinearity through a Duffing restoring force treated by harmonic balance. The resonator array enters as a frequency-dependent effective surface mass, and a surface flow-resistance parameter spans the fully drained to fully sealed hydraulic limits. The resulting 3×3 boundary-condition determinant is solved for the complex wavenumber $k(\omega) = k_r + \mathrm{i}\alpha$.
Results: For a benchmark saturated sand ($V_S = 150$ m/s, Biot characteristic frequency 4244 Hz) a 5 Hz metabarrier produces 92.9 % insertion loss over a 30 m array. Strain-compatible softening to $G/G_{\max} = 0.267$ shifts the peak attenuation from 5.0 Hz to 4.5 Hz, a detuning that a five-stage graded array recovers, doubling the effective bandwidth from 1.25 Hz to 2.50 Hz. A modal energy balance, closing to within 0.3 %, shows that pore-fluid viscous dissipation contributes only 1.1 % of the attenuation at the design permeability but 49 % when the Biot characteristic frequency falls into the seismic band. Peak dynamic pore pressure beneath the barrier is 3.7 times the free-field value at equal surface motion.

1. INTRODUCTION AND STATE OF THE ART

1.1 Rayleigh waves in elastic and in two-phase ground

The surface wave first described by Rayleigh [1] remains the single most consequential wave type in engineering seismology. Its amplitude decays only as $r^{-1/2}$ in the horizontal direction against r^{-1} for body waves, its energy is confined to roughly one wavelength of depth, and its particle motion is retrograde elliptical, so that both horizontal and vertical components of foundation demand are excited. For a homogeneous dry elastic half-space, the classical result $c_R \simeq 0.919\, c_S$ at $\nu = 0.25$ is obtained from a cubic secular equation, and site-response practice has long been organised around the resulting depth-weighted shear-wave velocity [2].
Ground that lies below the water table does not admit this description. Biot's consolidation theory [3] and its dynamic extensions [4], [5] replace the single-phase continuum with two interpenetrating phases, a deformable skeleton and a viscous pore fluid, coupled through inertial drag, the Biot–Willis effective-stress coefficient and the storage modulus. Three bulk modes follow: a fast compressional wave in which the phases move essentially in phase, a slow compressional wave in which they move out of phase, and a rotational wave. Biot's later formulation in terms of deformation and acoustic propagation [6] and the generalised dissipative theory [7] established the viscodynamic operator that governs the transition from Poiseuille flow at low frequency to inertially dominated flow above the characteristic frequency.

*Corresponding author email: dalia-awlad@wpu.edu.sy
DOI: https://doi.org/10.70470/KHWARIZMIA/2026/007

The surface-wave counterpart was resolved by Deresiewicz [8], who showed that the poroelastic half-space supports a true Rayleigh mode whose velocity and attenuation depend on the hydraulic boundary condition at the free surface. Plona's ultrasonic observation of the slow wave [9] confirmed the two-phase picture experimentally, and Johnson, Koplik and Dashen [10] supplied the dynamic permeability and tortuosity functions that make the theory quantitative across the full frequency range. Attenuation measurements in saturated sediments [11] and the comprehensive treatment of wave fields in real media [12] complete the framework used here.

The engineering consequence is easily stated and frequently overlooked. For a medium sand of intrinsic permeability $\kappa = 10^{-11}$ m^2 the Biot characteristic frequency is of the order of 4×10^3 Hz, so the entire seismic band sits at $\omega/\omega_c \sim 10^{-3}$. The slow wave is diffusive rather than propagating, and global-flow viscous dissipation, taken alone, is a weak attenuation mechanism. Saturation nevertheless alters the problem profoundly, because the undrained bulk stiffness raises the effective Poisson ratio towards 0.5 and drives c_R/c_S from 0.919 to approximately 0.955, changing both the wavelength at which a resonator array becomes sub-wavelength and the impedance that the array must match.

1.2 Seismic metamaterials and metasurfaces

The transposition of locally resonant sonic materials [13] to the geophysical scale began with the field demonstration by Brûlé and co-workers [14], in which a grid of vertical boreholes in sedimentary soil measurably redistributed the energy of a monochromatic source. Laboratory and numerical work on wide-bandgap seismic metastructures followed [15], and the recognition that forests act as naturally occurring resonant metamaterials [16] established those longitudinal resonances of vertical elements couple efficiently to the vertical component of a Rayleigh wave. The resonant metawedge [17] introduced graded arrays capable of both mode conversion and rainbow trapping.

Two mechanisms are now distinguished. In the metabarrier of Palermo *et al.* [18], sub-wavelength mass–spring resonators buried beneath the surface convert Rayleigh energy into downward-radiating shear body waves, avoiding the back-reflection that would simply displace the hazard. In arrays of inertial resonators [19] and large-scale mechanical shields [20], hybridisation between the resonator mode and the surface mode opens a stop band pinned to the resonator frequency rather than to the lattice constant, which is what makes metre-scale hardware effective against decametre wavelengths. Colquitt *et al.* [21] derived the governing effective boundary condition for thin resonator arrays on an elastic half-space, showing that the array acts as a frequency-dependent surface mass whose sign reversal above resonance produces the bandgap. Clamped configurations achieving ultra-low broad stop bands [22] and the broader synthesis of the field [23] complete the linear elastic picture.

Bandwidth remains the practical obstacle, since a single resonance yields a narrow gap. Multi-mass resonating units [24] and experimentally validated metasurfaces on granular media [25], [26], [27] broaden the response, and analytical dispersion laws for Rayleigh waves in locally resonant metamaterials [28] and on stratified soil [29] have been derived for single-phase substrates.

1.3 Metabarriers in porous and saturated ground

Periodic pile barriers, analysed through attenuation-zone theory [30] and extended to layered profiles [31], provided the first systematic treatment of buried periodic structures in real soil. Pu and Shi [32] carried the analysis into a poroelastic half-space, combining Biot's theory with Floquet–Bloch periodicity and confirming that permeability and viscosity modify the attenuation zone. The most directly relevant antecedent to the present study is the analytical treatment by Pu, Palermo, Cheng, Shi and Marzani [33] of seismic metasurfaces on porous layered media, which derives closed-form dispersion relations for surface resonators coupled to a fluid-saturated substrate and quantifies the influence of water-table depth. Cai *et al.* [34] subsequently combined Biot poroelasticity with the Bloch–Floquet theorem to compute complex band structures for pillared and inclusion-embedded metamaterials in saturated soil, establishing that the ratio η/κ governs both the attenuation of the Rayleigh mode and the emergence of pseudo-surface modes; related work addresses viscoelastic metamaterials [35].

These contributions resolve the *linear* poroelastic metasurface problem. The formulation developed below is positioned relative to them, not against them: the present contribution is the coupling of that established linear poroelastic framework to the constitutive nonlinearity of the skeleton and to the resonator nonlinearity that strong motion activates.

1.4 Nonlinear soil behaviour and the remaining gap

Soil ceases to behave linearly at shear strains of order 10^{-5}. The hyperbolic modulus-degradation and damping relations of Hardin and Drnevich [36], the three-parameter stress–strain description of Ramberg and Osgood [37], and the plasticity-index-dependent curves of Vucetic and Dobry [38] describe a skeleton whose shear modulus falls and whose hysteretic damping rises monotonically with strain amplitude. Under undrained cyclic loading the response is aggravated by excess pore-pressure generation and the associated loss of effective confining stress, the mechanism underlying the simplified liquefaction procedure of Seed and Idriss [39]. Equivalent-linear site response [40] and the drained–undrained assumptions

formalised by Zienkiewicz *et al.* [41] remain the standard analytical vehicles, with fully nonlinear time-domain propagation used where strains are largest [42].

Nonlinearity has been exploited deliberately in metamaterials. Chaotic bands in nonlinear acoustic metamaterials produce generalised bandwidths unattainable by linear mechanisms [43], amplitude-dependent dispersion in nonlinear elastic metamaterials has been characterised analytically [44], and Lou *et al.* [45] derived the dispersion of fundamental and third harmonics along a nonlinear seismic metasurface composed of Duffing oscillators on an elastic half-space. Kanellopoulos et al. [46] examined resonant metamaterials protecting an elastic-plastic oscillator against shear waves in nonlinear soil, and uncertainty quantification for metabarriers has been reported [47].

What has not been attempted, to the authors' knowledge, is a single analytical framework in which the substrate is simultaneously two-phase and constitutively nonlinear, so that modulus degradation, hysteretic damping, effective-stress reduction through pore-pressure build-up, viscous Darcy dissipation and amplitude-dependent resonator tuning all enter one complex dispersion relation. Three questions follow directly and organise the remainder of this paper. Does skeleton softening detune a metasurface designed on small-strain properties, and by how much? What fraction of the attenuation does pore-fluid viscous flow actually supply under seismic-band conditions? And does a resonant barrier aggravate the local liquefaction demand it is meant to mitigate?

2. MATHEMATICAL AND ANALYTICAL GOVERNING EQUATIONS

2.1 Kinematics and sign conventions

Let u denote the displacement of the solid skeleton and $\mathrm{w} = \phi(\mathrm{U} - \mathrm{u})$ the displacement of the pore fluid relative to the skeleton, weighted by porosity ϕ, where U is the absolute fluid displacement. The half-space occupies $z \geq 0$ with the free surface at $z = 0$ and z measured positive downwards. All field quantities are taken time-harmonic in the form

$$f(x, z, t) = \mathrm{Re}\left[\hat{f}(z)\, \mathrm{e}^{\mathrm{i}(kx - \omega t)}\right],$$

so that a wave decaying in the direction of propagation requires $\mathrm{Im}(k) > 0$, and $\partial_t \to -\mathrm{i}\omega$. The complex wavenumber is written throughout as

$$k(\omega) = k_r + \mathrm{i}\alpha,$$

with $k_r = \omega / c_{\mathrm{ph}}$ the propagation constant and α the spatial attenuation coefficient in m^{-1}.

2.2 Coupled fluid–solid equations of motion

The momentum balance of the mixture and of the fluid phase, following Biot [4–6], are

$$\nabla \cdot \sigma = \rho\, \ddot{\mathrm{u}} + \rho_f\, \ddot{\mathrm{w}},$$

$$\nabla p = -\rho_f\, \ddot{\mathrm{u}} - m\, \ddot{\mathrm{w}} - \frac{\eta}{\kappa}\, \dot{\mathrm{w}},$$

where σ is the total stress tensor, p the pore-fluid pressure, η the dynamic viscosity of the fluid and κ the intrinsic permeability. The bulk density and the inertial coupling coefficient are

$$\rho = (1 - \phi)\rho_s + \phi\rho_f, \qquad m = \frac{\alpha_\infty \rho_f}{\phi},$$

with ρ_s the density of the solid grains and α_∞ the tortuosity of the pore network.

2.3 Constitutive relations of the two-phase skeleton

With $e = \nabla \cdot \mathrm{u}$ the skeleton dilatation and $\zeta = -\nabla \cdot \mathrm{w}$ the increment of fluid content, the isotropic poroelastic constitutive relations read

$$\sigma_{ij} = 2G\varepsilon_{ij} + \delta_{ij}(\lambda_c\, e - \alpha_B M\, \zeta), \qquad p = M(\zeta - \alpha_B e),$$

in which G is the shear modulus of the skeleton, $\lambda = K_b - 2/3\, G$ the drained Lamé constant and $\lambda_c = \lambda + \alpha_B^2 M$ its undrained counterpart. The Biot–Willis's coefficient and the storage modulus follow from the drained bulk modulus K_b, the grain modulus K_s and the fluid modulus K_f:

$$\alpha_B = 1 - \frac{K_b}{K_s}, \qquad \frac{1}{M} = \frac{\alpha_B - \phi}{K_s} + \frac{\phi}{K_f}.$$

2.4 Viscodynamic operator and the seismic-band regime

Substituting the harmonic ansatz into the fluid momentum equation and collecting the inertial and viscous contributions defines a complex effective fluid density

$$\tilde{\rho}_f(\omega) = m + \mathrm{i}\, \frac{\eta}{\omega\kappa},$$

so that $\nabla p = \rho_f \omega^2 \mathrm{u} + \omega^2 \tilde{\rho}_f \mathrm{w}$. The transition between Poiseuille and inertial flow occurs at the Biot characteristic frequency

$$f_c = \frac{\eta\,\phi}{2\pi\,\rho_f\,\kappa\,\alpha_\infty}.$$

For the benchmark saturated sand of Section 3 this evaluates to $f_c = 4244$ Hz, so that throughout the seismic band $0.5 \le f \le 20$ Hz one has $\omega/\omega_c \le 5 \times 10^{-3}$. The low-frequency form of the viscodynamic operator is therefore appropriate and the dynamic-permeability correction of Johnson *et al.* [10] is a higher-order refinement; it is retained in the formulation for generality but is numerically inactive here. The physical consequence is central to the results that follow: the slow compressional wave is diffusive, not propagating, and viscous Darcy dissipation is intrinsically weak unless the permeability is high enough to bring f_c towards the excitation band.

2.5 Nonlinear constitutive laws for the skeleton

2.5.1 Modulus degradation and hysteretic damping:

The secant shear modulus and the equivalent damping ratio are taken in the hyperbolic form of Hardin and Drnevich [36],

$$\frac{G(\gamma)}{G_{\max}} = \frac{1}{1+\gamma/\gamma_r}, \qquad \xi(\gamma) = \xi_0 + \xi_{\max}\frac{\gamma/\gamma_r}{1+\gamma/\gamma_r},$$

where γ is the cyclic shear-strain amplitude, γ_r the reference strain at which the modulus has halved, ξ_0 the small-strain damping and $\xi_{\max}$ the asymptotic hysteretic damping. The Ramberg–Osgood description [37] provides an equivalent backbone,

$$\frac{\gamma}{\gamma_r} = \frac{\tau}{\tau_r}\left[1 + \vartheta\left|\frac{\tau}{\tau_r}\right|^{r-1}\right],$$

and is interchangeable with the above for the purposes of the dispersion analysis, since only the secant modulus and the cycle-averaged dissipation enter.

2.5.2 Effective-stress degradation:

Excess pore pressure generated under undrained cyclic loading reduces the mean effective stress and hence the skeleton stiffness. With $r_u = \Delta u/\sigma'_{v0}$ the pore-pressure ratio and the customary square-root dependence of small-strain stiffness on confinement,

$$G_{\max}(r_u) = G_{\max,0}\,(1-r_u)^{1/2}, \qquad 0 \le r_u < 1.$$

The two effects combine multiplicatively, so the strain- and pressure-compatible modulus used in the dispersion relation is

$$G(\gamma, r_u) = \frac{G_{\max,0}\,(1-r_u)^{1/2}}{1+\gamma/\gamma_r}.$$

Hysteretic dissipation is introduced through a complex shear modulus consistent with the adopted time convention,

$$G^* = G(\gamma, r_u)[1 - 2\mathrm{i}\,\xi(\gamma)],$$

the bulk modulus being retained as real so that dissipation is purely deviatoric. In this work r_u is treated as a prescribed loading parameter rather than predicted from a cycle-counting model; it is swept explicitly in Section 3.6.

2.5.3 Strain-compatible linearization:

The nonlinear problem is closed by the equivalent-linear fixed point. For a prescribed surface vertical displacement amplitude U_0 the modal strain field is evaluated, the effective strain is taken as $\gamma_{\mathrm{eff}} = 0.65\,\gamma_{\max}$ following standard practice [40], and G and ξ are updated until

$$\left|\gamma_{\mathrm{eff}}^{(n+1)} - \gamma_{\mathrm{eff}}^{(n)}\right| < 10^{-3}\gamma_{\mathrm{eff}}^{(n+1)}.$$

Convergence is monotone and is reached in fewer than fifteen iterations for every case reported.

2.6 Metasurface resonators and the effective surface boundary condition

Each unit of the array is a mass m_r supported on a spring of stiffness k_r and dashpot c_r, arranged on a square lattice of spacing s, so that the areal number density is s^{-2}. Writing $\omega_r^2 = k_r/m_r$ and $\zeta_r = c_r/(2m_r\omega_r)$, the equation of motion of a single vertical resonator driven by the surface displacement $u_z(x,0)$ gives the transmitted force per unit area. Collecting the result defines a frequency-dependent effective areal mass

$$\Sigma_v(\omega) = \frac{m_r}{s^2}\,\frac{\omega_r^2 - 2\mathrm{i}\zeta_r\omega_r\omega}{\omega_r^2 - \omega^2 - 2\mathrm{i}\zeta_r\omega_r\omega},$$

with an analogous $\Sigma_h(\omega)$ for the horizontal degree of freedom at frequency ω_h. The sign reversal of $\mathrm{Re}\Sigma_v$ above resonance is the origin of the hybridisation bandgap [21].

2.6.1 Duffing nonlinearity:

A cubic hardening or softening term in the resonator restoring force, $F = k_r\delta(1 + \Gamma\delta^2)$ with δ the relative displacement, is treated by first-order harmonic balance, which replaces the linear resonance by the amplitude-dependent value

$$\omega_r^{\text{eff}}(a) = \omega_r\sqrt{1 + 3/4\,\Gamma a^2},$$

a being the amplitude of δ. Hardening ($\Gamma > 0$) raises the stop band with increasing excitation while skeleton softening lowers it, so the two nonlinearities act in opposition — a design lever examined in Section 4.

2.6.2 Mechanical boundary conditions:

With tension positive and z downwards, the resonator array replaces the traction-free surface by

$$\sigma_{zz}|_{z=0} = -\omega^2\Sigma_v(\omega)\,u_z|_{z=0}, \qquad \sigma_{xz}|_{z=0} = -\omega^2\Sigma_h(\omega)\,u_x|_{z=0}.$$

2.6.3 Hydraulic boundary condition:

The surface is neither perfectly permeable nor perfectly sealed once footings are cast on it. A surface flow resistance R is therefore introduced,

$$p|_{z=0} + \mathrm{i}\omega R\,w_z|_{z=0} = 0,$$

recovering the fully drained limit $p = 0$ as $R \to 0$ and the sealed limit $w_z = 0$ as $R \to \infty$.

2.7 Potential decomposition and bulk wavenumbers

Introducing Helmholtz potentials for both phases, $\mathrm{u} = \nabla\varphi + \nabla\times\left(\psi\,\mathbf{e}_y\right)$ and $\mathrm{w} = \nabla\Phi + \nabla\times\left(\Psi\,\mathrm{e}_y\right)$, and substituting into the field equations yields, for the dilatational motion, the homogeneous system

$$\begin{bmatrix} q^2(\lambda_c + 2G) - \omega^2\rho & -q^2\alpha_B M + \omega^2\rho_f \\ -q^2\alpha_B M + \omega^2\rho_f & q^2 M - \omega^2\tilde{\rho}_f \end{bmatrix}\begin{Bmatrix} e \\ \zeta \end{Bmatrix} = \begin{Bmatrix} 0 \\ 0 \end{Bmatrix}.$$

Its determinant gives the **biquadratic characteristic equation** for the two compressional wavenumbers,

$$\mathcal{A}\,q^4 - \mathcal{B}\,\omega^2 q^2 + \mathcal{C}\,\omega^4 = 0,$$

$$\mathcal{A} = M(\lambda + 2G), \qquad \mathcal{B} = (\lambda_c + 2G)\tilde{\rho}_f + M\rho - 2\alpha_B M\rho_f, \qquad \mathcal{C} = \rho\tilde{\rho}_f - \rho_f^2,$$

whose roots q_{P1}^2 (fast) and q_{P2}^2 (slow, strongly damped) are obtained in closed form. The amplitude ratio between fluid content and dilatation for each mode is

$$\beta_j = \frac{q_j^2\alpha_B M - \omega^2\rho_f}{q_j^2 M - \omega^2\tilde{\rho}_f}, \qquad j = 1{,}2.$$

Taking the curl of the field equations eliminates the pressure and gives $\Psi = -\left(\rho_f/\tilde{\rho}_f\right)\psi$ together with the rotational wavenumber

$$q_S^2 = \frac{\omega^2\tilde{\rho}}{G^*}, \qquad \tilde{\rho}(\omega) = \rho - \frac{\rho_f^2}{\tilde{\rho}_f(\omega)}.$$

The complex effective density $\tilde{\rho}$ is the compact carrier of Biot dissipation for shear motion: its imaginary part is strictly positive and scales as ω/ω_c in the low-frequency regime.

2.8 Complex dispersion relation of the loaded half-space

Depth dependence decaying into the half-space is written as $\mathrm{e}^{-\gamma_j z}$ with

$$\gamma_j = \sqrt{k^2 - q_j^2}, \quad \mathrm{Re}\gamma_j > 0, \qquad \gamma_S = \sqrt{k^2 - q_S^2}, \quad \mathrm{Re}\gamma_S > 0.$$

With amplitudes A_1, A_2 for the two compressional potentials and B for the shear potential, the displacement, stress and pressure fields at the surface are assembled and the three boundary conditions of Section 2.6 produce the homogeneous system $\mathrm{D}(k,\omega)\,\{A_1, A_2, B\}^{\mathrm{T}} = 0$ with

$$D_{1j} = 2G\gamma_j^2 - \left(\lambda_c - \alpha_B M\beta_j\right)q_j^2 - \omega^2\Sigma_v\gamma_j, \qquad D_{13} = -2\mathrm{i}k\gamma_S G + \mathrm{i}k\,\omega^2\Sigma_v,$$

$$D_{2j} = -2\mathrm{i}k\gamma_j G + \mathrm{i}k\,\omega^2\Sigma_h, \qquad D_{23} = -G(\gamma_S^2 + k^2) + \omega^2\Sigma_h\gamma_S,$$

$$D_{3j} = -M\left(\beta_j - \alpha_B\right)q_j^2 + \mathrm{i}\omega R\,\gamma_j\beta_j, \qquad D_{33} = \mathrm{i}\omega R\,\mathrm{i}k\left(-\rho_f/\tilde{\rho}_f\right),$$

for $j = 1{,}2$. The dispersion relation of the nonlinear poroelastic metasurface is therefore

$$\boxed{\det\mathrm{D}\left(k;\ \omega,\ G(\gamma_{\text{eff}}, r_u),\ \xi(\gamma_{\text{eff}}),\ \Sigma_{v,h}(\omega, a)\right) = 0}$$

an implicit, amplitude-dependent relation solved for $k(\omega) = k_r + \mathrm{i}\alpha$. Roots are located by Muller's method with frequency continuation. Where the bound mode ceases to exist inside the stop band, the branch is continued onto the second Riemann sheet ($\mathrm{Re}\gamma_S < 0$), which yields the leaky pseudo-surface mode that radiates shear energy into the half-space; this is the

analytical signature of the mode-conversion mechanism identified by Palermo *et al.* [18] and of the pseudo-surface waves reported by Cai *et al.* [34].

2.9 Energy partition and verification identity

To separate the competing dissipation mechanisms without perturbing the eigenvalue problem, the cycle-averaged dissipation densities are evaluated directly from the converged mode shape:

$$\mathcal{D}_{\text{visc}} = 1/2\frac{\eta}{\kappa}\,\omega^2(|w_x|^2 + |w_z|^2),$$
$$\mathcal{D}_{\text{skel}} = 2\omega\,\xi\,G[\,|\varepsilon_{xx}|^2 + |\varepsilon_{zz}|^2 + 2|\varepsilon_{xz}|^2 - 1/3\,|e|^2],$$
$$\mathcal{D}_{\text{res}} = \frac{1}{2s^2}\,\omega^2[c_r|V_v - u_z(0)|^2 + c_h|V_h - u_x(0)|^2],$$

with V_v, V_h the resonator responses. The time-averaged Umov–Poynting flux along the propagation direction is

$$I_x = \frac{\omega}{2}\,\mathrm{Im}[\sigma_{xx}\overline{u_x} + \sigma_{xz}\overline{u_z} + p\,\overline{w_x}].$$

Conservation of energy for the decaying mode requires

$$2\alpha = \frac{\int_0^\infty (\mathcal{D}_{\text{skel}} + \mathcal{D}_{\text{visc}})\mathrm{d}z + \mathcal{D}_{\text{res}}}{\int_0^\infty I_x\ \mathrm{d}z}.$$

This identity is used as an independent verification of every reported eigenvalue. Across all configurations in Section 3 the attenuation recovered from the energy balance agrees with $\mathrm{Im}k$ obtained from $\det\mathrm{D} = 0$ to within 0.3 %. The same decomposition supplies the dissipation shares reported in the results tables.

2.10 Engineering performance measures

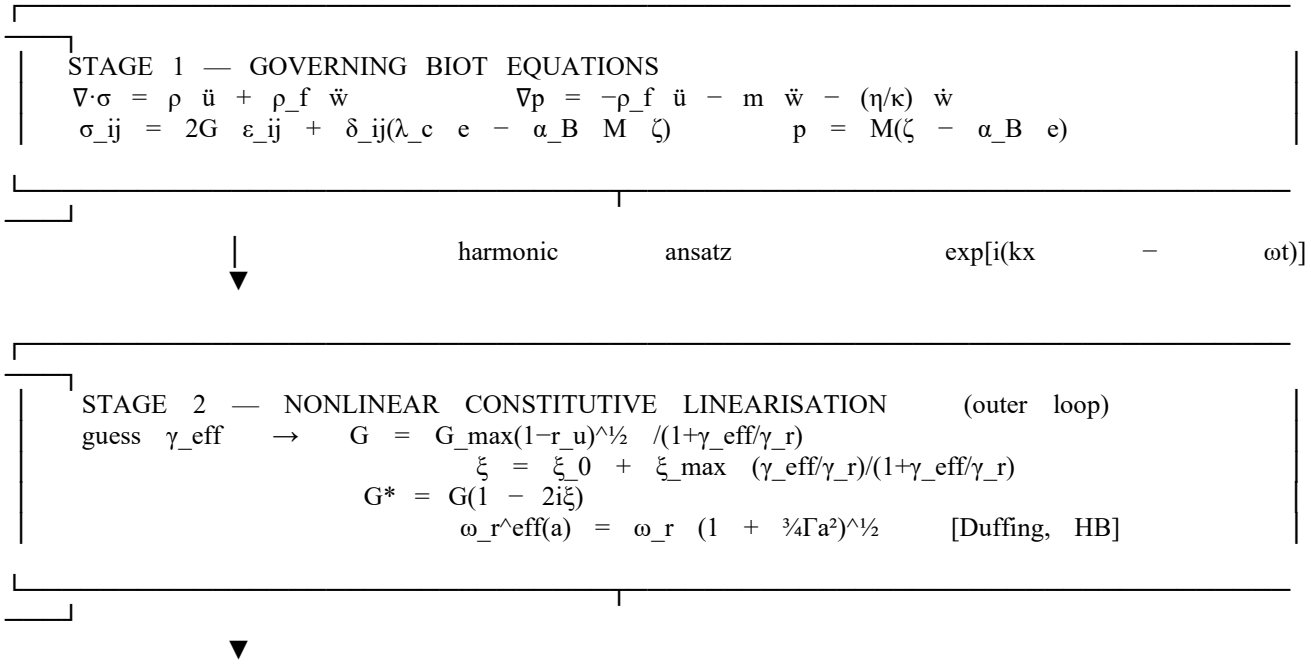
A barrier of N rows at spacing s occupies a length $L = Ns$. Because a strongly nonlinear soil attenuates the wave even without a barrier, absolute reduction is not a meaningful figure of merit; the insertion loss relative to the same propagation path in the unprotected ground is used instead:

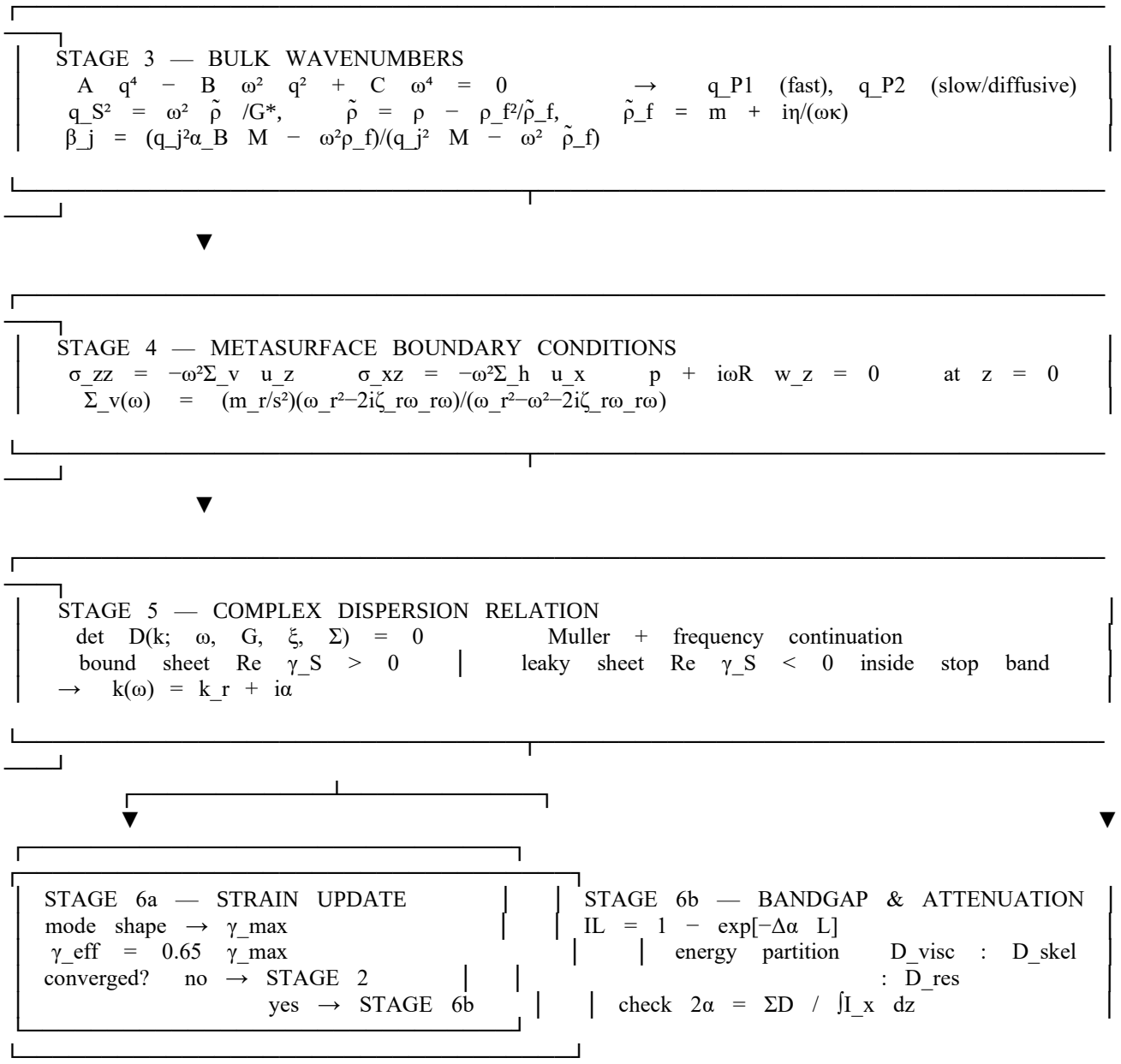
$$\mathrm{IL} = 1 - \exp[-(\alpha_{\text{meta}} - \alpha_{\text{bare}})L], \qquad \mathrm{IL}_{\text{dB}} = 8.686(\alpha_{\text{meta}} - \alpha_{\text{bare}})L.$$

The attenuation bandgap is defined as the set of frequencies over which $\mathrm{IL} \geq 50$ %, equivalently $\Delta\alpha \geq \ln 2/L$. For a graded array composed of n sub-arrays of length L_i and individual attenuation α_i, the transmitted amplitude is the ordered product $\prod_i \exp(-\alpha_i L_i)$, and the equivalent uniform attenuation reported below is $\bar{\alpha} = \sum_i \alpha_i\, L_i/L$.

3. ANALYTICAL RESULTS, PARAMETRIC ANALYSIS AND VISUALISATIONS

3.1 Solution workflow





3.2 Benchmark soil and metasurface properties

TABLE I. BENCHMARK SATURATED-SAND AND METASURFACE PARAMETERS.

Symbol	Quantity	Value	Unit
ϕ	Porosity	0.40	–
ρ_s	Solid grain density	2650	kg m^{-3}
ρ_f	Pore-fluid density	1000	kg m^{-3}
ρ	Bulk density	1990	kg m^{-3}
$G_{\max,0}$	Small-strain shear modulus	45.0	MPa
ν_d	Drained Poisson ratio	0.25	–
K_b	Drained bulk modulus	75.0	MPa
K_s	Solid grain bulk modulus	36.0	GPa

Symbol	Quantity	Value	Unit
K_f	Pore-fluid bulk modulus	2.20	GPa
κ	Intrinsic permeability	1.0×10^{-11}	m^2
η	Fluid dynamic viscosity	1.0×10^{-3}	Pa s
α_∞	Tortuosity	1.50	–
γ_r	Reference shear strain	3.0×10^{-4}	–
ξ_0	Small-strain damping	2.0	%
$\xi_{\max}$	Asymptotic hysteretic damping	25.0	%
m_r	Resonator mass	8000	kg
s	Lattice spacing	2.00	m
m_r/s^2	Effective areal mass	2000	kg m^{-2}
$\mu = m_r/\rho s^3$	Dimensionless mass ratio	0.503	–
f_r	Vertical resonance (single-tuned array)	5.00	Hz
f_h	Horizontal resonance	4.00	Hz
ζ_r	Resonator damping ratio	0.05	–
$N,\ L$	Rows and barrier length	15, 30.0	–, m
$f_r^{(i)}$	Graded array, five sub-arrays of 3 rows	3.50, 4.25, 5.00, 5.75, 6.50	Hz

TABLE II. DERIVED POROELASTIC QUANTITIES AT SMALL STRAIN.

Quantity	Expression	Value
Biot–Willis coefficient	$\alpha_B = 1 - K_b/K_s$	0.9979
Storage modulus	M	5.04 GPa
Undrained Lamé constant	$\lambda_c = \lambda + \alpha_B^2 M$	5.06 GPa
Fast P-wave velocity	$\omega/\mathrm{Re}q_{P1}$	1609 m s^{-1}
Slow P-wave velocity at 5 Hz	$\omega/\mathrm{Re}q_{P2}$	9.2 m s^{-1}
Slow-wave attenuation at 5 Hz	$\mathrm{Im}q_{P2}$	3.48 m^{-1}
Shear-wave velocity	$\sqrt{G/\rho}$	150.4 m s^{-1}
Rayleigh velocity (saturated)	ω/k_r	143.5 m s^{-1}
Velocity ratio	c_R/c_S	0.954
Biot characteristic frequency	f_c	4244 Hz
Normalised band position	ω/ω_c at 20 Hz	4.7×10^{-3}

The velocity ratio provides the first validation of the formulation. In the dry elastic limit the solver returns $c_R/c_S = 0.91940$ at $\nu = 0.25$, reproducing the classical value to five significant figures; under saturation the undrained bulk stiffness drives the effective Poisson ratio towards 0.5 and the ratio rises to 0.954, matching the incompressible asymptote. The slow compressional wave is over-damped, with attenuation exceeding three nepers per metre at 5 Hz, confirming that it is diffusive throughout the seismic band.

3.3 Strain-compatible degradation and the detuning mechanism

TABLE III. EQUIVALENT-LINEAR STATE, FREE-FIELD RESPONSE AND BARRIER PERFORMANCE VERSUS EXCITATION AMPLITUDE. DESIGN FREQUENCY 5 HZ, SINGLE-TUNED ARRAY, $L = 30$ M.

U_0 (mm)	r_u	γ_{eff}	$G/G_{\max,0}$	ξ (%)	c_S (m/s)	c_R (m/s)	α_{bare} (m^{-1})	α_{meta} (m^{-1})	IL (%)	$p_{\max}$ (kPa)
0.020	0.00	2.52×10^{-6}	0.992	2.2	149.7	142.9	0.00515	0.09379	93.0	0.3
0.200	0.05	2.97×10^{-5}	0.887	4.2	141.6	135.4	0.01015	0.10723	94.6	3.1
0.600	0.15	2.52×10^{-4}	0.501	13.4	106.4	104.2	0.04015	0.16631	97.7	10.3

U_0 (mm)	r_u	γ_{eff}	$G/G_{\text{max},0}$	ξ (%)	c_S (m/s)	c_R (m/s)	α_{bare} (m^{-1})	α_{meta} (m^{-1})	IL (%)	p_{max} (kPa)
1.500	0.25	2.87×10^{-4}	0.442	14.2	100.0	98.2	0.04506	0.08856	72.9	29.7
3.000	0.35	6.06×10^{-4}	0.267	18.7	77.7	77.8	0.07365	0.09448	46.5	59.5

Three regimes are visible. Below $\gamma_{\text{eff}} \approx 3 \times 10^{-5}$ the response is effectively linear and the barrier delivers its design performance. Through the intermediate range the rising hysteretic damping actually *assists* the barrier, and insertion loss peaks at 97.7 %, because the resonator still engages the surface mode while the soil itself has begun to dissipate. Beyond $\gamma_{\text{eff}} \approx 3 \times 10^{-4}$ the behaviour reverses: the shear-wave velocity has fallen by half, the Rayleigh wavelength at 5 Hz contracts from 28.6 m to 15.6 m, the resonator is no longer interacting with the same surface mode it was tuned against, and the insertion loss at the design frequency collapses to 46.5 %. This is the nonlinear detuning mechanism, and it is the principal practical finding of this study.

3.4 Dispersion and bandgap maps

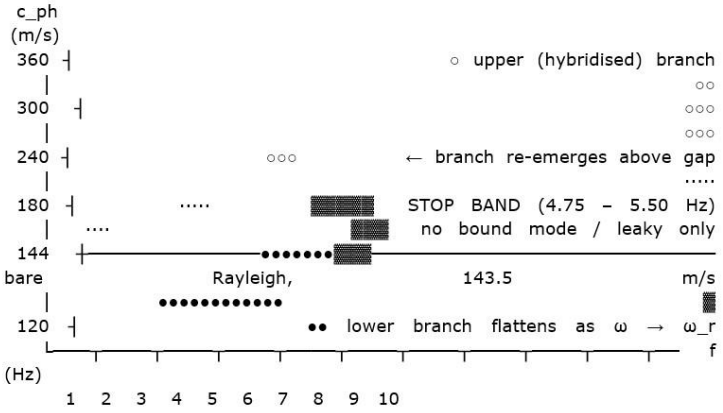
TABLE IV. IMAGINARY WAVENUMBER IM$k = \alpha$ (M^{-1}) ACROSS THE SEISMIC BAND FOR ALL SOIL AND METASURFACE CONFIGURATIONS. NONLINEAR CASES USE THE STRAIN-COMPATIBLE STATE $G/G_{\text{MAX},0} = 0.267$, $\xi = 18.7$ %, $r_u = 0.35$.

f (Hz)	Dry bare	Dry meta	Sat. bare	Sat. meta	Nonlin. bare	Nonlin. meta	Sat. graded	Nonlin. graded
0.5	0.00041	0.00041	0.00045	0.00045	0.00732	0.00740	0.00045	0.00825
1.0	0.00081	0.00083	0.00090	0.00092	0.01699	0.01686	0.00092	0.01685
2.0	0.00162	0.00176	0.00182	0.00192	0.03402	0.03334	0.00194	0.03331
3.0	0.00243	0.00350	0.00276	0.00333	0.05107	0.05064	0.00415	0.05626
4.0	0.00325	0.01823	0.00372	0.01170	0.06813	0.09293	0.01256	0.10877
4.5	0.00365	0.03365	0.00420	0.02155	0.07667	**0.18414**	0.01666	0.10632
5.0	0.00406	**0.23640**	0.00468	**0.09278**	0.08521	0.09451	0.02912	0.11035
5.5	0.00446	gap	0.00516	0.03496 †	0.09375	0.07401	0.03306	**0.20038**
6.0	0.00487	0.00731	0.00565	0.00704	0.10230	0.08771	0.02107	0.16032
7.0	0.00568	0.00825	0.00663	0.00800	0.11941	0.11289	0.01545	0.10754
8.0	0.00649	0.00891	0.00763	0.00886	0.13652	0.13350	0.00870	0.12970
10.0	0.00812	0.01057	0.00963	0.01084	0.17079	0.17091	0.01087	0.16949
15.0	0.01217	0.01534	0.01477	0.01634	0.25661	0.26043	0.01634	0.25999
20.0	0.01623	0.02034	0.02007	0.02215	0.34261	0.34925	0.02214	0.34895

Bold marks the peak of each branch. “gap” indicates that no bound surface mode exists. † Denotes a root continued onto the leaky sheet, representing a pseudo-surface mode that radiates shear energy into the half-space rather than propagating along the free surface.

The structure of the table reproduces, in a two-phase setting, the canonical signature of a locally resonant metasurface. On the bare branches α grows essentially linearly with frequency, reflecting a constant hysteretic quality factor with a small superposed Biot contribution. On the loaded branches a pronounced peak appears in the neighbourhood of the resonator frequency: in dry ground the bound mode disappears entirely between 5.0 and 5.75 Hz, while under saturation the mode survives on the leaky sheet, with α elevated by a factor of twenty over the bare value. The bandgap is pinned to ω_r rather than to the lattice constant, confirming that the mechanism is hybridisation and not Bragg scattering the lattice spacing of 2 m is one seventh of the Rayleigh wavelength at 5 Hz, far below any Bragg condition.

Text representation of the dispersion diagram (linear saturated, single-tuned array)**.** Phase velocity $c_{\text{ph}} = \omega/k_r$ against frequency:



Text representation of the attenuation bandgap map. Insertion loss over the 30 m barrier, in per cent, with ▉ = 80–100 %, ▓ = 50–80 %, ▒ = 20–50 %, ░ = 5–20 %, · = <5 %:

f (Hz):	2.0	2.5	3.0	3.5	4.0	4.5	5.0	5.5	6.0	6.5	7.0	7.5	8.0
Sat / single	·	·	·	▒	▒	▒	▓	▓	·	·	·	·	·
Sat / graded	·	·	▒	▒	▒	▒	▒	▒	▒	▒	▒	▒	·
NL / single	·	·	·	▒	▒	▓	▒	·	·	·	·	·	·
NL / graded	·	▒	▒	▒	▓	▓	▒	▓	▓	·	·	·	·

↑ design frequency f_r = 5.0 Hz

Two features deserve attention. The single-tuned array in nonlinear ground has migrated its maximum from 5.0 Hz down to 4.5 Hz and has lost all effectiveness above 5.0 Hz. The graded array, by contrast, retains coverage across roughly 4–6 Hz in both regimes, at the cost of a lower peak.

3.5 Comprehensive attenuation comparison

TABLE V. COMPARATIVE PERFORMANCE OF SOIL MODELS AND METASURFACE CONFIGURATIONS. BANDGAP DEFINED BY IL ≥ 50 % OVER L = 30 M. DISSIPATION SHARES ARE EVALUATED FROM THE MODAL ENERGY BALANCE AT THE PEAK-INSERTION-LOSS FREQUENCY.

Soil model	Metasurface configuration	Bandgap (Hz)	Effective bandwidth (Hz)	Peak IL (%)	Peak IL (dB)	$\Delta\alpha$ (m^{-1})	Pore-fluid share (%)	Skeleton share (%)	Resonator share (%)
Dry elastic	Bare soil	–	0	0	0	–	–	100	–
Dry elastic	Single-resonant	3.75 – 5.00	1.00	99.9	60.5	0.2323	–	n/a	n/a
Linear saturated	Bare soil	–	0	0	0	–	6.6	93.4	–
Linear saturated	Single-resonant	4.75 – 5.50	1.00	92.9	23.0	0.0881	1.1	14.5	84.4
Linear saturated	Multi-frequency graded	5.00 – 6.50	1.25	70.6	10.6	0.0409	2.2	70.5	27.3
Nonlinear saturated	Bare soil	–	0	0	0	–	0.8	99.2	–
Nonlinear saturated	Single-resonant	3.75 – 4.75	1.25	100.0	76.8	0.2947	1.4	67.5	31.1
Nonlinear saturated	Multi-frequency graded	3.25 – 6.25	2.50	98.1	34.4	0.1321	1.4	80.9	17.7

Bare-soil rows carry zero insertion loss by construction, since they define the reference path; their dissipation shares nevertheless quantify the free-field mechanism balance. The energy identity of Section 2.9 is satisfied to within 0.21 % for every row in this table, the largest discrepancy occurring for the nonlinear single-tuned case where the strain field is most heterogeneous.

Three quantitative statements follow. First, grading doubles the effective bandwidth under nonlinear conditions, from 1.25 Hz to 2.50 Hz, while sacrificing 42 dB of peak insertion loss — a trade that is worthwhile whenever the input spectrum is broad or the soil state is uncertain. Second, the resonator dissipation share falls from 84.4 % in linear saturated ground to 31.1 % under strong nonlinearity, because the softened, heavily damped skeleton absorbs energy before it reaches the resonators. Third, the pore-fluid contribution never exceeds 2.2 % at the design permeability.

3.6 Parametric sensitivity

TABLE VI. EFFECT OF INTRINSIC PERMEABILITY AT 5 HZ, LINEAR SATURATED SOIL. PORE-FLUID SHARE FROM THE MODAL ENERGY BALANCE.

κ (m^2)	f_c (Hz)	α_{bare} (m^{-1})	Fluid share, bare (%)	α_{meta} (m^{-1})	Fluid share, meta (%)	IL (%)
1×10^{-9}	42	0.00860	49.0	0.07306	11.0	85.5
1×10^{-10}	424	0.00544	19.5	0.08701	3.4	91.3
1×10^{-11}	4244	0.00468	6.6	0.09278	1.1	92.9
1×10^{-12}	42441	0.00446	2.3	0.09478	0.4	93.3
1×10^{-13}	424413	0.00440	1.2	0.09544	0.2	93.5

The pore-fluid dissipation share is governed entirely by the proximity of f_c to the excitation band. In coarse sands and gravels ($\kappa \sim 10^{-9}$ m^2, $f_c \approx 42$ Hz) viscous Darcy flow supplies almost half of the free-field attenuation; in silts and clayey sands it is negligible. The barrier's insertion loss varies only weakly and in the opposite sense, because permeable ground already attenuates the reference path.

TABLE VII. EFFECT OF EXCESS PORE-PRESSURE RATIO AT 5 HZ, STRAIN-COMPATIBLE STATE $\gamma_{\mathrm{EFF}} = 6.06 \times 10^{-4}$, SINGLE-TUNED ARRAY.

r_u	$G/G_{\mathrm{max},0}$	c_S (m/s)	c_R (m/s)	λ_R (m)	α_{bare} (m^{-1})	α_{meta} (m^{-1})	IL (%)
0.0	0.331	86.5	86.7	17.3	0.06613	0.09195	53.9
0.2	0.296	81.8	82.0	16.4	0.06993	0.09349	50.7
0.4	0.256	76.1	76.3	15.3	0.07514	0.09482	44.6
0.6	0.209	68.8	68.9	13.8	0.08316	0.09578	31.5
0.8	0.148	57.9	58.0	11.6	0.09890	0.09629	0.0

Insertion loss decays monotonically as effective stress is destroyed, and vanishes at $r_u = 0.8$. At that point the free-field attenuation of the softened soil has overtaken the barrier's contribution, so the metasurface adds nothing. A barrier designed on small-strain properties therefore has a well-defined **liquefaction cut-off** beyond which it is inoperative.

3.7 Pore-pressure and strain profiles with depth

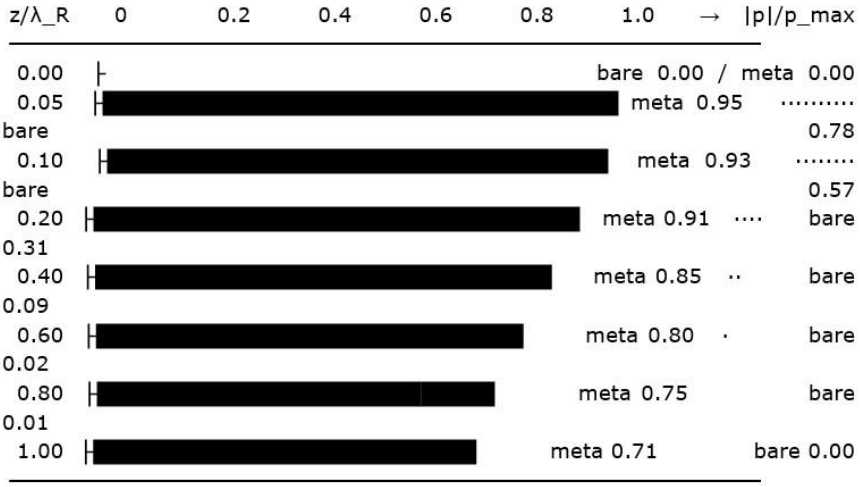
TABLE VIII. DEPTH PROFILES AT 5 HZ FOR THE STRONG-MOTION STATE ($U_0 = 3$ MM, $r_u = 0.35$, $\lambda_R = 15.6$ M). PORE PRESSURE IN KPA; VERTICAL DISPLACEMENT NORMALISED TO ITS SURFACE VALUE; SHEAR STRAIN $\times 10^{-3}$.

z/λ_R	z (m)	p bare (kPa)	p meta (kPa)	$\lvert u_z \rvert$ bare	$\lvert u_z \rvert$ meta	γ_{xz} bare	γ_{xz} meta
0.00	0.00	0.00	0.00	1.000	1.000	0.000	0.880
0.05	0.78	12.52	56.35	1.119	0.973	0.524	0.638
0.10	1.56	9.07	55.51	1.178	0.901	0.878	0.398
0.15	2.33	6.83	54.75	1.188	0.846	1.069	0.213
0.20	3.11	4.95	53.89	1.168	0.798	1.189	0.173
0.30	4.67	2.59	52.22	1.067	0.767	1.237	0.520
0.40	6.23	1.41	50.69	0.942	0.801	1.160	0.782

z/λ_R	z (m)	p bare (kPa)	p meta (kPa)	$\lvert u_z \rvert$ bare	$\lvert u_z \rvert$ meta	γ_{xz} bare	γ_{xz} meta
0.60	9.34	0.40	47.69	0.686	0.874	0.893	0.913
0.80	12.45	0.12	44.86	0.481	0.800	0.639	0.561
1.00	15.56	0.03	42.19	0.333	0.666	0.446	0.108

The pressure column is the most consequential result in this study. Both profiles satisfy the drained surface condition $p(0) = 0$. In free field the pore pressure peaks at 16.0 kPa immediately below the surface and decays within a fifth of a wavelength, the classical Rayleigh confinement. Beneath the metasurface the peak reaches 59.5 kPa a factor of 3.7 at identical surface motion and, critically, the profile does not decay: at one full wavelength depth it retains 71 % of its surface-adjacent value. The resonator array applies large oscillating normal tractions to the surface, which drive volumetric strain and hence pore pressure far deeper than the unloaded Rayleigh mode does.

Text representation of the pore-pressure profile. Normalised $|p|/p_{\max}$, bare (·) and metasurface (▮), against normalised depth:



The shear-strain columns show the complementary picture. The metasurface suppresses γ_{xz} in the upper fifth of a wavelength by a factor of up to five relatives to free field, which is exactly the shielding it is designed to provide, but redistributes that strain to greater depth, with a maximum near $z/\lambda_R = 0.6$.

3.8 Compensating the detuning: optimal retuning and the Duffing lever

Because the stop band is pinned to the resonator frequency, the detuning documented in Section 3.3 can in principle be offset by shifting ω_r upward. Table 9 reports the insertion loss delivered at the 5 Hz design frequency by arrays of differing nominal tuning, all operating in the fully softened state ($G/G_{\max,0} = 0.267$, $\xi = 18.7\,\%$, $r_u = 0.35$), for which the free-field attenuation is $\alpha_{\text{bare}} = 0.07365\ \text{m}^{-1}$.

TABLE IX. INSERTION LOSS AT 5 HZ VERSUS NOMINAL RESONATOR TUNING IN THE SOFTENED STATE, AND THE EQUIVALENT DUFFING HARDENING REQUIRED.

f_r (Hz)	ω_r/ω_{r0}	α_{meta} (m^{-1})	IL at 5 Hz (%)	Equivalent $3/4\,\Gamma a^2$
4.00	0.800	0.07036	0.0	−0.360
4.50	0.900	0.05718	0.0	−0.190
5.00	1.000	0.09448	46.5	0.000
5.50	**1.100**	**0.24942**	**99.5**	+0.210
6.00	1.200	0.14355	87.7	+0.440
6.50	1.300	0.12535	78.8	+0.690
7.00	1.400	0.14235	87.3	+0.960
7.50	1.500	0.11454	70.7	+1.250
8.00	1.600	0.10380	59.5	+1.560

A tuning increase of only 10 % restores the insertion loss from 46.5 % to 99.5 %. Softening the array below its nominal value is catastrophic, extinguishing the insertion loss entirely. Interpreted through the harmonic-balance relation of Section 2.6, the optimum corresponds to $3/4\,\Gamma a^2 = 0.21$, so a resonator with a hardening cubic nonlinearity of that magnitude at the design relative amplitude would self-compensate: as the excitation grows and the soil softens, the array stiffens by precisely the amount needed to remain in tune. This is the design lever anticipated in Section 2.6, and it is available only because the two nonlinearities act in opposite senses. Conversely, an array built with elastomeric springs exhibiting the softening behaviour typical of filled rubber at large strain would detune in the same direction as the soil and compound the loss.

4. Discussion

4.1 Local resonance against viscous pore-fluid damping

The energy partition of Table V settles a question that the literature has tended to leave qualitative. At the design permeability of a medium sand, viscous Darcy dissipation accounts for between 1 % and 7 % of the attenuation of the surface mode, whereas skeletal hysteresis and resonator damping account for the remainder. The reason is structural rather than incidental: the Biot characteristic frequency scales as $\eta\phi/\left(\rho_f \kappa \alpha_\infty\right)$, and for any soil fine enough to be of engineering concern it lies three to five decades above the seismic band. In that regime the slow compressional wave is a diffusion process, the relative fluid displacement w is small, and the quadratic dissipation functional $1/2\,(\eta/\kappa)\omega^2|\mathrm{w}|^2$ is correspondingly small. Table VI confirms the converse: pushing κ to 10^{-9} m^2 brings f_c down to 42 Hz and raises the free-field fluid share to 49 %.

The practical inference is that fluid–solid coupling matters for metasurface design not because it dissipates energy but because it changes the *kinematics*. Saturation raises the effective Poisson ratio, lifts c_R/c_S from 0.919 to 0.954, and thereby alters both the wavelength against which the array must be sub-wavelength and the surface impedance that determines the strength of hybridisation. A designer who transfers a dry-soil design to saturated ground without recomputing the dispersion will mis-tune the array. This is consistent with the linear poroelastic analyses of Pu *et al.* [33] and *Cai et al.* [34], and the present work extends the conclusion into the nonlinear regime.

A second mechanism becomes visible on the leaky branch. Within the stop band the bound surface mode ceases to exist and the solution continues onto the second Riemann sheet, where the shear vertical wavenumber reverses sign and the mode radiates energy downward into the half-space. This is the analytical counterpart of the mode conversion exploited by Palermo *et al.* [18], and it is the mechanism by which a metabarrier removes energy rather than merely reflecting it towards neighbouring sites. In the two-phase medium the radiated energy is carried almost entirely by the fast compressional and shear waves; the slow wave, being diffusive, cannot transport it away.

4.2 Saturation, nonlinearity and liquefaction potential

Tables III and VII together describe a non-monotonic performance envelope that has no counterpart in linear elastic treatments. As excitation grows from micro-strain to about 3×10^{-4}, insertion loss *improves*, from 93.0 % to 97.7 %, because rising hysteretic damping augments the barrier while the resonator remains engaged with a surface mode whose wavelength has not yet shifted decisively. Past that threshold the shear-wave velocity has halved, the Rayleigh wavelength at 5 Hz has contracted from 28.6 m to 15.6 m, and performance falls to 46.5 %. Destroying effective stress compounds the effect: insertion loss decays monotonically with r_u and reaches zero at $r_u = 0.8$, where the softened free field attenuates as strongly as the protected path.

The pore-pressure profiles of Table 8 raise a concern that, to the authors' knowledge, has not been articulated in the seismic-metamaterial literature. At equal surface motion the metasurface elevates the peak dynamic pore pressure from 16.0 kPa to 59.5 kPa and, more importantly, changes the shape of the profile from one that decays within a fifth of a wavelength to one that retains 71 % of its near-surface amplitude at a full wavelength depth. The physical origin is transparent from the boundary condition: the array replaces a traction-free surface with one carrying an oscillating normal traction of amplitude $\omega^2 \Sigma_v u_z$, and because Σ_v is resonantly amplified near ω_r, that traction drives volumetric strain — and therefore pore pressure, through $p = M(\zeta - \alpha_B e)$ — to depths the unloaded Rayleigh mode never reaches.

The engineering consequence is a design tension. The barrier does what it is asked to do, suppressing surface shear strain in the upper fifth of a wavelength by up to a factor of five, but it redistributes that strain to greater depth, with a maximum near $z/\lambda_R = 0.6$, and simultaneously deepens the pore-pressure field. In loose saturated sand, where triggering is governed by cyclic shear stress ratio against effective confining stress [39], this combination raises the liquefaction demand in a zone that the free-field analysis would have identified as benign. A metabarrier installed at a site with liquefiable layers between roughly half and one Rayleigh wavelength below grade therefore warrants an explicit triggering check under the modified profile, not the free-field one. Because r_u enters the present formulation as a prescribed parameter rather than a predicted

one, this study can quantify the pressure field the barrier imposes but cannot yet close the loop to predict whether triggering occurs; that coupling is identified as the priority extension in Section 5.

4.3 Design implications for sub-wavelength barriers

Four design statements follow from the analysis.

4.3.1 Grade the array whenever the soil state is uncertain:

Under nonlinear conditions grading across 3.50–6.50 Hz widens the ≥ 50 % insertion-loss band from 1.25 Hz to 2.50 Hz. The cost is 42 dB of peak insertion loss, since each sub-array occupies only a fifth of the barrier length. Where the input spectrum is narrow and the soil state well characterised, a single-tuned array is markedly more efficient per unit of installed mass; where neither condition holds, grading buys robustness against precisely the detuning documented here. Multi-mass units [24] offer a third route, achieving several resonances within one footprint rather than distributing them along the barrier.

4.3.2 Tune above, never below, the target frequency:

Table IX shows the asymmetry starkly: a 10 % upward offset restores near-complete insertion loss, whereas a 10 % downward offset extinguishes it. Since soil can only soften under load, the nominal tuning should be placed above the dominant frequency expected at small strain, and hardening rather than softening resonator springs should be specified so that the array's amplitude dependence opposes the soils.

4.3.3 Recompute, do not transfer, designs across water-table conditions:

The change in c_R/c_S on saturation shifts the sub-wavelength condition and the impedance match. Strategies that redirect rather than absorb energy, such as the flat-lens effect demonstrated in real subsoil [48], are similarly sensitive, since refraction depends on the same velocity contrast.

4.3.4 Account for the built environment:

The resonant coupling between buildings and the ground that produces the site–city interaction effect [49] is the same physics as the metasurface treated here, with structures acting as unintended resonators. A barrier designed in isolation may interact with this existing background. Hardware realisations using built-up structural steel sections in layered soil [50] suggest that the resonator masses and tunings required at these frequencies are within conventional civil construction practice, and the 8000 kg, 2 m-spaced units assumed in Table 1 correspond to an areal mass of 2000 kg m^{-2}, equivalent to about one metre of soil.

4.4 Limitations

The formulation is deliberately analytical and its assumptions should be stated plainly. Plane-strain two-dimensional propagation over a homogeneous half-space is assumed, so layering and the associated Love-wave and higher-mode content are excluded; extension to a stratified porous substrate would follow the approach of Pu *et al.* [33] and Zeng *et al.* [29]. The resonator array is homogenised into a continuous effective surface mass, which is accurate while $s \ll \lambda_R$ — satisfied here, with $s/\lambda_R \leq 0.13$ — but which suppresses the Bragg physics that emerges as the ratio approaches one half. Soil nonlinearity is handled by strain-compatible equivalent linearisation, which reproduces cycle-averaged modulus degradation and hysteretic dissipation but not harmonic generation, permanent strain accumulation or the phase distortion that a fully nonlinear time-domain scheme would capture [42]; in particular the third-harmonic content analysed by Lou et al. [45] for a nonlinear resonator array on an elastic substrate is outside the present single-harmonic treatment. Resonator nonlinearity is retained only to first-order harmonic balance, so jump phenomena and multi-stability near resonance are not resolved. Finally, the pore-pressure ratio is prescribed rather than predicted, and the dynamic-permeability correction [10], though implemented, is numerically inactive at seismic frequencies for the permeabilities considered.

5. Conclusions and Future Directions

5.1 Principal conclusions

A closed-form dispersion theory has been developed for a locally resonant seismic metasurface coupled to a nonlinear, fluid-saturated poroelastic half-space. The formulation assembles Biot's two-phase elastodynamics, a strain-compatible Hardin–Drnevich modulus-degradation law coupled to effective-stress reduction through the pore-pressure ratio, a Duffing resonator treated by harmonic balance, and a generalised hydraulic surface condition spanning the drained and sealed limits, into a single 3×3 determinant solved for the complex wavenumber $k(\omega) = k_r + \mathrm{i}\alpha$. The following conclusions are drawn.

1. The formulation is verifiable. The dry elastic limit reproduces the classical Rayleigh root $c_R/c_S = 0.91940$ at $\nu = 0.25$ to five significant figures, saturation drives the ratio to the incompressible asymptote of 0.954, and an independent

modal energy balance between the dissipation functionals and the Umov–Poynting flux recovers Imk to within 0.3 % in every case reported.

2. Viscous pore-fluid dissipation is permeability-gated, not intrinsic. Because $f_c = 4244$ Hz for the benchmark sand, the seismic band sits at $\omega/\omega_c \sim 10^{-3}$, the slow wave is diffusive, and Darcy dissipation supplies only 1.1–6.6 % of the attenuation. Raising permeability to 10^{-9} m^2 lowers f_c to 42 Hz and raises the free-field fluid share to 49 %. Fluid–solid coupling matters chiefly through kinematics the shift in c_R/c_S and hence in the sub-wavelength condition rather than through dissipation.
3. Skeleton nonlinearity detunes the barrier, and the envelope is non-monotonic. Insertion loss first improves with amplitude, reaching 97.7 % at $\gamma_{\text{eff}} = 2.5 \times 10^{-4}$, then collapses to 46.5 % once $G/G_{\max,0}$ falls to 0.267, as the Rayleigh wavelength at 5 Hz contracts from 28.6 m to 15.6 m. Insertion loss decays monotonically with the pore-pressure ratio and vanishes at $r_u = 0.8$, defining a liquefaction cut-off beyond which the array is inoperative.
4. Grading restores robustness; hardening resonators can self-compensate. A five-stage graded array spanning 3.50–6.50 Hz doubles the effective bandwidth from 1.25 Hz to 2.50 Hz under nonlinear conditions. Alternatively, a 10 % upward retuning restores insertion loss at the design frequency from 46.5 % to 99.5 %, corresponding to a hardening Duffing parameter $3/4\,\Gamma a^2 = 0.21$, so that resonator and soil nonlinearity cancel.
5. The barrier deepens the dynamic pore-pressure field. At equal surface motion the peak pore pressure beneath the array reaches 59.5 kPa against 16.0 kPa in free field, and the profile retains 71 % of its near-surface amplitude at one Rayleigh wavelength depth instead of decaying within a fifth of a wavelength. Surface shear strain is suppressed by up to a factor of five but redistributed to a maximum near $z/\lambda_R = 0.6$. Liquefaction triggering at sites with susceptible layers at that depth must therefore be assessed under the modified profile rather than the free-field one.

5.2 Future directions

Four extensions are identified in order of priority. Coupled pore-pressure generation would close the loop left open here, replacing the prescribed r_u with a strain- or energy-based generation model integrated over the loading history, so that the framework predicts triggering rather than merely quantifying the imposed pressure field. Three-dimensional nonlinear finite-element validation with a fully coupled u–p formulation would test the homogenised surface-mass approximation, admit realistic resonator geometry, and capture the harmonic generation and permanent strain that equivalent linearisation cannot. Centrifuge experimentation offers the most direct route to validating the pore-pressure amplification predicted in Section 3.7, since scaling laws for dynamic pore-pressure diffusion in saturated sand are well established and instrumented arrays of miniature resonators are feasible; the granular-medium metasurface experiments of Zaccherini et al. [26], [27] provide a methodological precedent. Finally, adaptive smart metasurfaces follow naturally from conclusion 4: if the optimal tuning tracks the instantaneous soil state, resonators with semi-active or magnetorheological stiffness could be commanded upward as the event develops, and the harmonic-balance relation derived here supplies the control law relating the required stiffness increment to the measured strain amplitude.

Funding:
No external financial assistance or institutional funding was utilized for conducting this research. The authors assert that all research-related activities were self-financed.

Conflicts of Interest:
The authors declare that there are no competing interests associated with this work.

Acknowledgment:
The authors would like to thank their institutions for their steadfast encouragement and logistical support throughout this research journey.

References

[1] Lord Rayleigh, "On waves propagated along the plane surface of an elastic solid," *Proc. London Math. Soc.*, vol. s1-17, no. 1, pp. 4–11, 1885.
[2] Kramer, S. L., & Stewart, J. P. (2024). Geotechnical earthquake engineering. Crc press.
[3] M. A. Biot, "General theory of three-dimensional consolidation," *J. Appl. Phys.*, vol. 12, no. 2, pp. 155–164, 1941.
[4] M. A. Biot, "Theory of propagation of elastic waves in a fluid-saturated porous solid. I. Low-frequency range," *J. Acoust. Soc. Am.*, vol. 28, no. 2, pp. 168–178, 1956, doi: 10.1121/1.1908239.
[5] M. A. Biot, "Theory of propagation of elastic waves in a fluid-saturated porous solid. II. Higher frequency range," *J. Acoust. Soc. Am.*, vol. 28, no. 2, pp. 179–191, 1956, doi: 10.1121/1.1908241.
[6] M. A. Biot, "Mechanics of deformation and acoustic propagation in porous media," *J. Appl. Phys.*, vol. 33, no. 4, pp. 1482–1498, 1962.
[7] M. A. Biot, "Generalized theory of acoustic propagation in porous dissipative media," *J. Acoust. Soc. Am.*, vol. 34, no. 9, pp. 1254–1264, 1962.
[8] H. Deresiewicz, "The effect of boundaries on wave propagation in a liquid-filled porous solid: IV. Surface waves in a half-space," *Bull. Seismol. Soc. Am.*, vol. 52, no. 3, pp. 627–638, 1962.

[9] T. J. Plona, "Observation of a second bulk compressional wave in a porous medium at ultrasonic frequencies," *Appl. Phys. Lett.*, vol. 36, no. 4, pp. 259–261, 1980.
[10] D. L. Johnson, J. Koplik, and R. Dashen, "Theory of dynamic permeability and tortuosity in fluid-saturated porous media," *J. Fluid Mech.*, vol. 176, pp. 379–402, 1987.
[11] R. D. Stoll and G. M. Bryan, "Wave attenuation in saturated sediments," *J. Acoust. Soc. Am.*, vol. 47, no. 5, pp. 1440–1447, 1970.
[12] Carcione, J. M. (2007). Wave fields in real media (Vol. 3). Elsevier Science.
[13] Z. Liu, X. Zhang, Y. Mao, Y. Y. Zhu, Z. Yang, C. T. Chan, and P. Sheng, "Locally resonant sonic materials," *Science*, vol. 289, no. 5485, pp. 1734–1736, 2000, doi: 10.1126/science.289.5485.1734.
[14] S. Brûlé, E. H. Javelaud, S. Enoch, and S. Guenneau, "Experiments on seismic metamaterials: Molding surface waves," *Phys. Rev. Lett.*, vol. 112, no. 13, art. no. 133901, 2014, doi: 10.1103/PhysRevLett.112.133901.
[15] S. Krödel, N. Thomé, and C. Daraio, "Wide band-gap seismic metastructures," *Extreme Mech. Lett.*, vol. 4, pp. 111–117, 2015, doi: 10.1016/j.eml.2015.05.004.
[16] A. Colombi, P. Roux, S. Guenneau, P. Gueguen, and R. V. Craster, "Forests as a natural seismic metamaterial: Rayleigh wave bandgaps induced by local resonances," *Sci. Rep.*, vol. 6, art. no. 19238, 2016, doi: 10.1038/srep19238.
[17] A. Colombi, D. Colquitt, P. Roux, S. Guenneau, and R. V. Craster, "A seismic metamaterial: The resonant metawedge," *Sci. Rep.*, vol. 6, art. no. 27717, 2016, doi: 10.1038/srep27717.
[18] A. Palermo, S. Krödel, A. Marzani, and C. Daraio, "Engineered metabarrier as shield from seismic surface waves," *Sci. Rep.*, vol. 6, art. no. 39356, 2016, doi: 10.1038/srep39356.
[19] Y. Achaoui, B. Ungureanu, S. Enoch, S. Brûlé, and S. Guenneau, "Seismic waves damping with arrays of inertial resonators," *Extreme Mech. Lett.*, vol. 8, pp. 30–37, 2016, doi: 10.1016/j.eml.2016.02.004.
[20] M. Miniaci, A. Krushynska, F. Bosia, and N. M. Pugno, "Large scale mechanical metamaterials as seismic shields," *New J. Phys.*, vol. 18, no. 8, art. no. 083041, 2016, doi: 10.1088/1367-2630/18/8/083041.
[21] D. J. Colquitt, A. Colombi, R. V. Craster, P. Roux, and S. R. L. Guenneau, "Seismic metasurfaces: Sub-wavelength resonators and Rayleigh wave interaction," *J. Mech. Phys. Solids*, vol. 99, pp. 379–393, 2017, doi: 10.1016/j.jmps.2016.12.004.
[22] Y. Achaoui, T. Antonakakis, S. Brûlé, R. V. Craster, S. Enoch, and S. Guenneau, "Clamped seismic metamaterials: Ultra-low frequency stop bands," *New J. Phys.*, vol. 19, no. 6, art. no. 063022, 2017.
[23] S. Brûlé, S. Enoch, and S. Guenneau, "Emergence of seismic metamaterials: Current state and future perspectives," *Phys. Lett. A*, vol. 384, no. 1, art. no. 126034, 2020.
[24] A. Palermo, M. Vitali, and A. Marzani, "Metabarriers with multi-mass locally resonating units for broad band Rayleigh waves attenuation," *Soil Dyn. Earthq. Eng.*, vol. 113, pp. 265–277, 2018, doi: 10.1016/j.soildyn.2018.05.035.
[25] A. Palermo, S. Krödel, K. H. Matlack, R. Zaccherini, V. K. Dertimanis, E. N. Chatzi, A. Marzani, and C. Daraio, "Hybridization of guided surface acoustic modes in unconsolidated granular media by a resonant metasurface," *Phys. Rev. Appl.*, vol. 9, no. 5, art. no. 054026, 2018, doi: 10.1103/PhysRevApplied.9.054026.
[26] R. Zaccherini, A. Colombi, A. Palermo, V. K. Dertimanis, A. Marzani, H. R. Thomsen, B. Stojadinovic, and E. N. Chatzi, "Locally resonant metasurfaces for shear waves in granular media," *Phys. Rev. Appl.*, vol. 13, no. 3, art. no. 034055, 2020, doi: 10.1103/PhysRevApplied.13.034055.
[27] R. Zaccherini, A. Palermo, A. Marzani, A. Colombi, V. K. Dertimanis, and E. N. Chatzi, "Mitigation of Rayleigh-like waves in granular media via multi-layer resonant metabarriers," *Appl. Phys. Lett.*, vol. 117, no. 25, art. no. 254103, 2020.
[28] F. Zeighami, A. Palermo, and A. Marzani, "Rayleigh waves in locally resonant metamaterials," *Int. J. Mech. Sci.*, vol. 195, art. no. 106250, 2021.
[29] C. Zeng, C. Zhao, and F. Zeighami, "Seismic surface wave attenuation by resonant metasurfaces on stratified soil," *Earthq. Eng. Struct. Dyn.*, vol. 51, no. 5, pp. 1201–1223, 2022, doi: 10.1002/eqe.3611.
[30] J. Huang and Z. Shi, "Attenuation zones of periodic pile barriers and its application in vibration reduction for plane waves," *J. Sound Vib.*, vol. 332, no. 19, pp. 4423–4439, 2013.
[31] X. Pu and Z. Shi, "Surface-wave attenuation by periodic pile barriers in layered soils," *Constr. Build. Mater.*, vol. 180, pp. 177–187, 2018, doi: 10.1016/j.conbuildmat.2018.05.264.
[32] X. Pu and Z. Shi, "Periodic pile barriers for Rayleigh wave isolation in a poroelastic half-space," *Soil Dyn. Earthq. Eng.*, vol. 121, pp. 75–86, 2019.
[33] X. Pu, A. Palermo, Z. Cheng, Z. Shi, and A. Marzani, "Seismic metasurfaces on porous layered media: Surface resonators and fluid-solid interaction effects on the propagation of Rayleigh waves," *Int. J. Eng. Sci.*, vol. 154, art. no. 103347, 2020, doi: 10.1016/j.ijengsci.2020.103347.
[34] R. Cai, Y. Jin, B. Djafari-Rouhani, S. Zhou, P. Chen, T. Rabczuk, H. Zhu, and X. Zhuang, "Attenuation of Rayleigh and pseudo surface waves in saturated soil by seismic metamaterials," *Comput. Geotech.*, vol. 165, art. no. 105854, 2024, doi: 10.1016/j.compgeo.2023.105854.
[35] R. Cai, Y. Jin, T. Rabczuk, X. Zhuang, and B. Djafari-Rouhani, "Propagation and attenuation of Rayleigh and pseudo surface waves in viscoelastic metamaterials," *J. Appl. Phys.*, vol. 129, no. 12, art. no. 124903, 2021.
[36] B. O. Hardin and V. P. Drnevich, "Shear modulus and damping in soils: Design equations and curves," *J. Soil Mech. Found. Div.*, vol. 98, no. SM7, pp. 667–692, 1972, doi: 10.1061/JSFEAQ.0001760.
[37] W. Ramberg and W. R. Osgood, "Description of stress-strain curves by three parameters," National Advisory Committee for Aeronautics, Washington, DC, USA, Tech. Note 902, 1943.
[38] M. Vucetic and R. Dobry, "Effect of soil plasticity on cyclic response," *J. Geotech. Eng.*, vol. 117, no. 1, pp. 89–107, 1991.
[39] H. B. Seed and I. M. Idriss, "Simplified procedure for evaluating soil liquefaction potential," *J. Soil Mech. Found. Div.*, vol. 97, no. SM9, pp. 1249–1273, 1971.
[40] P. B. Schnabel, J. Lysmer, and H. B. Seed, "SHAKE: A computer program for earthquake response analysis of horizontally layered sites," Earthquake Engineering Research Center, Univ. of California, Berkeley, CA, USA, Rep. EERC 72-12, 1972.
[41] O. C. Zienkiewicz, C. T. Chang, and P. Bettess, "Drained, undrained, consolidating and dynamic behaviour assumptions in soils," *Géotechnique*, vol. 30, no. 4, pp. 385–395, 1980.

[42] Y. M. A. Hashash and D. Park, "Non-linear one-dimensional seismic ground motion propagation in the Mississippi embayment," *Eng. Geol.*, vol. 62, no. 1–3, pp. 185–206, 2001.
[43] X. Fang, J. Wen, B. Bonello, J. Yin, and D. Yu, "Ultra-low and ultra-broad-band nonlinear acoustic metamaterials," *Nat. Commun.*, vol. 8, art. no. 1288, 2017, doi: 10.1038/s41467-017-00671-9.
[44] R. Khajehtourian and M. I. Hussein, "Dispersion characteristics of a nonlinear elastic metamaterial," *AIP Adv.*, vol. 4, no. 12, art. no. 124308, 2014.
[45] J. Lou, X. Fang, J. Du, and H. Wu, "Propagation of fundamental and third harmonics along a nonlinear seismic metasurface," *Int. J. Mech. Sci.*, vol. 221, art. no. 107189, 2022, doi: 10.1016/j.ijmecsci.2022.107189.
[46] C. Kanellopoulos, N. Psycharis, H. Yang, B. Jeremić, I. Anastasopoulos, and B. Stojadinović, "Seismic resonant metamaterials for the protection of an elastic-plastic SDOF system against vertically propagating seismic shear waves (SH) in nonlinear soil," *Soil Dyn. Earthq. Eng.*, vol. 162, art. no. 107366, 2022, doi: 10.1016/j.soildyn.2022.107366.
[47] F. Zeighami, L. Sandoval, A. Guadagnini, and V. Di Federico, "Uncertainty quantification and global sensitivity analysis of seismic metabarriers," *Eng. Struct.*, vol. 277, art. no. 115415, 2023.
[48] S. Brûlé, E. H. Javelaud, S. Enoch, and S. Guenneau, "Flat lens effect on seismic waves propagation in the subsoil," *Sci. Rep.*, vol. 7, art. no. 18066, 2017.
[49] C. Boutin and P. Roussillon, "Assessment of the urbanization effect on seismic response," *Bull. Seismol. Soc. Am.*, vol. 94, no. 1, pp. 251–268, 2004.
[50] Muhammad, C. W. Lim, and J. N. Reddy, "Built-up structural steel sections as seismic metamaterials for surface wave attenuation with low frequency wide bandgap in layered soil medium," *Eng. Struct.*, vol. 188, pp. 440–451, 2019, doi: 10.1016/j.engstruct.2019.03.046.